Normalized Microwave Reflection Index:

A Vegetation Measurement derived from GPS Networks

Kristine M. Larson

Department of Aerospace Engineering Sciences, University of Colorado

Eric E. Small

Department of Geological Sciences, University of Colorado

Corresponding Author:

Kristine M. Larson

UCB 429

University of Colorado

Boulder, CO 80309

Kristinem.larson@gmail.com

303 492 6583 (phone)

303 492 7881 (fax)

Abstract

Measurements of vegetation state are required both for modeling and satellite validation. Reflected GPS signals recorded by the Plate Boundary Observatory network provide a source of new information about vegetation state in the western United States and Alaska. The GPS ground stations were installed between 2005-2008 to measure plate boundary deformation. They operate continuously and transmit their data to a public facility at least once/day. However, they also act as bi-static radars by recording the interference between a direct GPS signal (transmitted at 1.5 GHz) and a reflected GPS signal. This frequency of this interference pattern primarily depends on the vertical distance between the antenna and the ground reflector. As a L-band sensor, the amplitude of the interference pattern depends on vegetation water content. A daily vegetation metric that depends on reflection amplitudes, NMRI (Normalized Microwave Reflection Index), is defined. A method for removing outliers caused by snow and rain is described. The footprint of NMRI depends on the antenna height and local terrain. The minimum footprint is 1,000 m^2. A database of more than 300 station NMRI time series have been compiled; these data span the period 2007-2013. Comparisons between NMRI and *in situ* sampling of vegetation state are the subject of a companion paper.

1. Introduction

The amount of water stored in vegetation canopies is an important biophysical parameter for both climate studies and drought monitoring. For example, the productivity of natural and agricultural ecosystems is strongly controlled by plant water status [1]. Knowledge of the amount of biomass and its water content can guide fire management practices [2]. Quantifying the amount of water in plants is also critical for retrieval of hydrologic variables from remote sensing data - as both passive and active remote sensing of soil moisture requires knowledge of vegetation water content (VWC) [3,4]. Accordingly, remote sensing methods have been developed to estimate water in vegetation, using both optical and radar data.

There is a long history of using optical remote sensing to estimate biophysical parameters. The Normalized Difference Vegetation Index [5], and similar indices [6], has been calculated from operational satellite data for decades. NDVI is largely considered a measure of plant greenness, and has been used to infer biomass, leaf area index (LAI), fractional vegetation cover and other variables [7,8,9]. VWC has also been estimated from NDVI, although a cause-effect relationship does not exist between the two variables [10]. Factors such as plant type, plant-water status, and hydroclimatic conditions affect VWC and "greenness" differently, thus the relationship between NDVI and VWC is not expected to be strong [11].

An optical remote sensing index to more directly quantify the amount of water in vegetation is known as Normalized Difference Water Index (NDWI) [12]. It is calculated using reflectance in

two near infrared (NIR) channels. Similar indices have been proposed that use reflectance at other NIR wavelengths, either tuned for different satellite channels or to capitalize on other water absorption bands [2,13,14,15,10]. Validation of these indices by comparison to *in situ* observations demonstrates a range of performance, depending upon vegetation type, sensor configuration, and other factors. Reflection from the underlying soil complicates the use of NDWI and related indices in areas with fractional vegetation cover or low LAI [12,13,10].

Both passive and active microwave remote sensing have been used to estimate water stored in vegetation [16]. The dielectric constant of water is roughly ten times higher than for dry vegetation. Therefore, the amount of water stored in plant material directly affects how microwave radiation interacts with vegetation canopies, including changes in scattering, polarization, and absorption. The amount of water in vegetation affects the emissivity of the canopy, and thus the brightness temperature sensed remotely [17]. Water in vegetation also absorbs microwave radiation emitted by the soil surface, thus vegetation water content hinders retrieval of soil moisture via passive radar sensing [3]. Vegetation optical depth (VOD) can be retrieved from brightness temperature measurements. Comparisons between the seasonal evolution of VOD and NDVI show that there are both similarities and differences between these microwave and optical measures [18].

Active microwave experiments have shown that VWC and other biophysical parameters affect the scattering coefficient and polarization of signals from vegetation canopies. Various sensor configurations have been evaluated, including a range of wavelengths, polarizations, and incidence angles [19,20,21,22]. In general, the scattering coefficient increases as VWC and

biomass increase, with the greatest sensitivity at incidence angles of ~20-40 degrees off nadir. At L-band, radar backscatter is sensitive across a wide range of VWC (0-5 kg/m^2) [23]. L-band signals penetrate all but the thickest vegetation canopies (e.g., tropical forests), and therefore they are also affected by soil moisture [4]. In addition to soil moisture, the VWC-backscatter relationship is complicated by vegetation structure and soil surface roughness. The influence of these factors may be minimized by using the Radar Vegetation Index (RVI), which incorporates both cross- and co-polarized measurements [23,24].

A relatively new L-band remote sensing technique with relevance for measuring vegetation state uses reflected GPS (and more generally GNSS, Global Navigation Satellite Systems, signals). Reflected GPS signals were first proposed in 1993 as a method to measure sea level from space [25]. This idea has since been expanded and tested on a variety of ground, aircraft, and space based platforms for studies of soil moisture [26,27], altimetry [28,29], ocean winds [30], sea ice [31], oil slicks [32], ocean tides [33,34], and snow [35]. Most relevant to this study are the GPS reflection studies of [36,37,38] where the technique is applied to vegetation. These investigators showed that GPS signal power levels could be used to detect vegetation changes for a variety of agricultural crops, including corn, sorghum, wheat, barley, sunflowers, and leaves in walnut trees. Good agreement was shown between the GPS retrievals and field observations of vegetation height and VWC.

In this paper, we describe an alternative way to use GPS to measure VWC. An index is derived from these data, Normalized Microwave Reflection Index (NMRI). As with [36,37,38], a bistatic-radar geometry is used. L-band signals transmitted by GPS satellites are reflected by the

land surface and received by geodetic-quality GPS antennas a few meters above the ground. A limited number of comparisons between these types of GPS reflections and *in situ* observations of plant biophysical parameters were first presented by [39]; they also compared time series of GPS reflections and NDVI from several sites in the western United States. In this paper we summarize the theory that explains the reflected GPS signals, present a method to quantify reflections from the GPS observations, describe the data editing required for a useful metric, and provide a first-order normalization to correct for terrain effects. Validation of the NMRI method by comparison with *in situ* measurements of VWC is covered in a companion paper [40, hereafter paper II].

2. Overview of the Global Positioning System

NMRI is based on reflection effects (paper.) recorded in GPS ranging data, known as pseudoranges and carrier phases. The goal of this section is to first provide a description of the GPS system needed to define NMRI. This will be followed by a theoretical description of multipath geometry and how it can be observed in GPS measurements known as pseudoranges.

2.1 Satellites

GPS is a constellation of satellites (currently 31) at an altitude of ~20,000 km above the surface of the Earth. Each GPS satellite orbits the Earth with a ~12 hour orbital period, meaning that the ground tracks repeat at a nearly sidereal (23h:56m) period [41]. The satellites are separated into 6 orbital planes spaced at 60-degree intervals and inclined at an angle of 55 degrees with respect to the equator. As a result, GPS receivers in the continental U.S. can track anywhere from 6-12 GPS satellite signals at any given time. All GPS satellites transmit Right-Handed Circularly-Polarized (RHCP) signals at L-band. The primary GPS transmission frequencies (f_1 for the L_1

band and f_2 for the L_2 band) are 1.57542 and 1.22760 GHz; the equivalent L_1 and L_2 carrier wavelengths λ_1 and λ_2 are approximately 0.19 and 0.244 m.

The geometry of these GPS satellite tracks strongly depends on the receiver's latitude. Figure 1 displays the azimuth and elevation angle of all visible GPS satellites for a site located in southern Montana (Elevation is the angle of the satellite with respect to the local horizon). No observations are shown below 10 degrees for reasons that will be discussed in Section 3. While individual satellite tracks vary, the satellite highlighted in Figure 1A takes approximately 4 hours to rise and set, reaching a maximum elevation angle of ~45 degrees (Figure 1B). Longer satellite tracks – that reach higher elevation angles – generally correspond to ~6 hours in the western United States.

In North America there is a distinctive hole in GPS observations to the north, which is due to the inclination of the GPS orbit; there is an equivalent measurement hole in the south for GPS users in the southern hemisphere. Depending on which satellites are in which orbital planes and the user's location, a stationary GPS receiver will track a given GPS satellite once or twice per day. The location of GPS satellites within their orbital planes has varied somewhat over the past six years, but not in a way that significantly impacts the footprint of the GPS reflections.

2.2 Ground Networks

Starting in the mid-1980s, geodesists and geophysicists demonstrated that dual-frequency carrier-phase GPS instruments could be used to measure fault motions [42]. However, the cost of such receivers was prohibitive for permanent installations. As the price of GPS instrumentation decreased in the 1990s, geophysicists began deploying continuously-operating GPS instruments.

Data from these networks are typically downloaded once per day and made immediately available via the internet.

More than 3000 geodetic-quality GPS sites are currently operating in the United States. Many of these are operated by individual city, county, and state agencies. These GPS sites primarily support precise surveying activities; others are operated by the U.S. Geological Survey to support hazard studies for earthquakes and volcanoes. Universities have augmented these networks to study specific faults. In this study we use GPS data from the NSF EarthScope Plate Boundary Observatory (PBO) (Figure 2A). The locations of the PBO sites were chosen to facilitate scientific investigations of tectonic signals. Thus, there are a very large number of sites that follow the general outline of the San Andreas Fault in California. Likewise there are receivers across the Basin and Range that trend east to west because the fault zones in this area are oriented north-south. Clusters of instruments can also be seen at Yellowstone, Mt. St. Helens, and Mammoth Volcanoes. Although a large number of sites are located in urban areas, particularly near Los Angeles, over 90% are situated in natural environments. There are a total of 1100 GPS sites in the PBO network (See http://pbo.unavco.org for a current listing).

The GPS instrumentation at each PBO site is nearly identical (Figure 2B). The GPS receivers (the Trimble NetRS model) can track up to 12 GPS satellites at a time. The antenna is covered by an acrylic dome; the latter provides protection from the snow, leaves, dirt, etc. This "choke-ring" antenna is designed to preferentially receive RHCP signals from above the horizon, i.e. elevation angles greater than zero [43]. Most of the antennas deployed by PBO were mounted on a 2-meter tall tripod that was drilled into bedrock. Standard data retrievals are every 15 seconds.

While consistent receiver/antenna units were used at each site, the terrain at each site does vary significantly. The digital elevation map for a representative GPS site (P048) is provided in Figure 2C.

The PBO network was built between 2005-2008. Those initial years were valuable for identifying problems with the GPS hardware, telemetry, and receiver firmware. By late 2006, most of these issues had been resolved. The database described in this study begins on January 1, 2007 and extends through the end of 2013.

3. GPS Multipath - Theory

In order to estimate position, GPS units measure biased distances (ranges) from multiple satellites to the receiving antenna, measurements called pseudoranges and carrier phases. As a GPS antenna must be able to track multiple satellites from different directions in the sky, an "omni-directional" antenna is used. It is difficult to design an antenna that rejects all energy from reflected signals (i.e. those arriving from negative elevation angles) without negatively impacting the direct signals that arrive from positive elevation angles. The antenna used by geodesists is a compromise. The gain pattern is fairly homogeneous, which is important to geodesists because they want each antenna to have the same geometric phase center location. The antenna gain pattern was designed to strongly prefer RHCP over LHCP measurements so that direct signals (RHCP) would dominate over reflected signals (LHCP). For elevation angles above ~25 degrees and natural surfaces such as soil and snow, this antenna design is adequate. However, its efficiency breaks down at lower elevation angles for two reasons:

193 (1) The antenna RHCP gains are nearly equal for positive and negative elevation angles.
194 (2) Reflections from most natural land surfaces retain the polarization of the incident
195 vector electric field in the limit of grazing incidence.

196 For example, the Brewster angle is 10-25 degrees for bare soil, depending on whether it is wet or
197 dry. This is far different than what would be observed, for example, if the GPS antenna were
198 deployed over a large metal surface such as copper. In this case, the reflected energy at low
199 elevation angles would be LHCP and would be rejected by the antenna.

200 In addition to issues related to the antenna, reflected GPS signals are defined by their geometry
201 (Figure 3). The GPS antenna receives both direct and reflected energy and the receiver measures
202 the interference between them. To characterize the behavior of this "GPS interferometer," we
203 need to know the wavelength of the carrier signal and how well the two signals are synchronized
204 (i.e. its phase).

205 To determine the phase of the interference pattern, we first calculate the excess path delay D
206 generated by the reflection. Figure 3 shows the geometric representations of both the direct and
207 the reflected signals. For a horizontal planar reflector, it can be shown that D is:

208 (1)

$$D = 2H \sin e$$

209

210 where H is the height of the antenna above the reflecting surface and e is the elevation angle of
211 the satellite with respect to the horizon [44]. The phase φ_1 of the interference for a GPS carrier
212 wavelength λ_1 is then:

213

214

215 (2)

$$\varphi_1 = \frac{2\pi}{\lambda_1} D = \frac{4\pi H}{\lambda_1} \sin e$$

216

217 The frequency of the interference (also known as its modulation) is the time derivative of the

218 phase:

219

220 (3)

$$\frac{d\varphi_1}{dt} = \frac{d}{dt}\left(\frac{4\pi H}{\lambda_1} \sin e\right) = \frac{2\pi}{\lambda_1} 2\mathrm{H} \cos e \frac{de}{dt}$$

221

222

223 Equation 3 shows that the interferometric frequency will be greater for large H than small H, and

224 will change as the satellite rises (or sets).

225

226 A full derivation of multipath effects on GPS signals is beyond the scope of this paper. A short

227 summary is provided in Appendix 1. Pseudorange multipath error on the L1 frequency

228 (M_1) depends directly on excess path length D and is defined:

229

230 (4)

$$M_1 = \frac{\alpha \, \mathrm{D} \cos \varphi_1}{1 + \alpha \cos \varphi_1}$$

231

where α is a damping factor defined as the ratio between the reflected (multipath) amplitude (A_m) and the direct signal amplitude (A_d).

Both A_m and A_d depend strongly on elevation angle. The direct signal term A_d is mostly controlled by the antenna gain. It has several key characteristics in a geodetic GPS instrument:

1. The antenna gain for RHCP is many orders of magnitude stronger than for LHCP.
2. The antenna trades off tracking higher elevation satellites at the expense of lower elevation satellites; therefore A_d is smaller at low elevations than high elevations.
3. A_d depends on transmission power levels. However, this effect is much smaller than the antenna gain effect.

The reflection characteristics of the surface are encompassed in A_m. This is the parameter that is sensitive to vegetation water content: higher vegetation water content leads to lower A_m. For the choke ring antenna used by the PBO network (and using equation 4), one can predict the general characteristics of pseudorange multipath errors. Figure 4 shows multipath predictions for antennas at 3 different heights above a horizontal planar reflector. We can see that the dominant frequency in multipath errors depends directly on the height of the antenna above the reflecting surface (*H*), i.e. "far" reflectors have high frequencies and vice versa. Secondly, the amplitude of multipath also depends strongly on *H*, so that far reflectors have much larger amplitudes than near reflectors.

These multipath predictions shown in Figure 4 are very simplified in the sense that the model

255 uses a generic representation of α and because only a simple planar reflecting surface was used.
256 To fully model GPS multipath errors, the actual reflection coefficients of the surface must be
257 known (e.g. bare soil, surface roughness, soil type and wetness, characterization of the
258 vegetation), the gain of the antenna for both RHCP and LHCP must be defined, and the terrain
259 surrounding the antenna must be modeled. A simulator to make these types of model predictions
260 is under development, with initial efforts focusing on simple geometries and bare soil [50,51,52].
261 At the current time, we use the simple principles outlined in sections 3 to help us define a GPS
262 multipath metric (NMRI) that is sensitive to vegetation water content. In the next section we
263 define how GPS pseudorange multipath can be observed.

264 **4. GPS Multipath - Observations**

265 **4.1 Observable Equations**

266 There are two kinds of GPS observables: pseudoranges and carrier phases (carrier phase is *not*
267 the same as the interferometric phase discussed in the previous section). We first define the L_1
268 ranging observable P_1(pseudorange). For a given receiver and satellite and time, $P_1$is defined as:

269 (6)

270 $$P_1 = \rho + c\delta_r - c\delta_s + I/f_1^2 + T + M_1 + \varepsilon_1$$

271 The terms that depend on the transmit frequency have subscripts of 1 for the L_1 frequency. The
272 geometric range term ρ represents the path traveled by the signal from the satellite to the receiver
273 in a vacuum (i.e. the straight-line path). For a GPS receiver on the Earth this term varies from
274 ~22,000-25,000 km. δ represents clock errors for either the receiver or satellite; it is scaled by the

speed of light, c. Clock errors can easily produce error terms greater than 100 km (Note: relativistic effects have been subsumed into the satellite clock term). The ionospheric delay term (I) depends on how many electrons are along the path between the satellite and receiver and is scaled by the inverse square of the transmit frequency. The tropospheric delay T (gases and precipitable water vapor) also depends on the path between the receiver and the satellite, however, it is not frequency-dependent at GPS frequencies. For convenience, the frequency-scaled ionospheric and tropospheric error terms are shown as having units of meters. The measurement error term is shown as ε_1. M_1 is the pseudorange multipath term described in section 3 and the parameter of interest in this study. We must remove as many terms as possible from equation 6 in order to isolate M_1. Although not used in this paper, we note that there is a pseudorange observable on the L_2 frequency.

The codes (used to define the pseudoranges) are transmitted on carrier signals. The phases of these carrier signals can be converted into very precise, biased ranges. The carrier phase observables (ϕ_1 and ϕ_2) are very similar to P_1:

(7)

$$\lambda_1 \, \phi_1 \; = \rho + c\delta_r - c\delta_s - I/f_1^2 + T + m_1 + N_1 \; \lambda_1 \; + \varepsilon_\phi$$

(8)

$$\lambda_2 \, \phi_2 \; = \rho + c\delta_r - c\delta_s \quad - I/f_2^2 + T + m_2 + N_2 \; \lambda_2 \; + \varepsilon_\phi$$

N_1 and N_2 are known as carrier phase ambiguities. These must be estimated for positioning applications. The terms can change due to "cycle slips" or "loss of lock," meaning new values must be estimated. To mitigate their impact, only data above elevation angles above 10 degrees

are used in this study. The measurement error term for carrier phase (ε_ϕ) is several mm and much smaller than that of pseudorange (ε_1 ~25-30 cm). Note that the ionospheric error for carrier phase data has the opposite sign as for pseudorange. Carrier phase multipath errors (m_1 and m_2) are bounded to be one quarter of the carrier phase wavelength, ~5 cm. The geometric range, clock errors, and tropospheric errors are identical for carrier phase and pseudorange data.

The reader will note that simply subtracting $\lambda_1\varphi_1$ from P_1 would isolate pseudorange multipath, but at the expense of doubling the ionospheric error. If however P_1 and both carrier phase observables are used, one can isolate pseudorange multipath and remove the ionospheric error. This observable - MP_1 - is frequently used in the geodetic community because it has no dependence on orbits, clocks, or atmospheric delays:

(9)

$$MP_1 = P_1 - \frac{f_1^2 + f_2^2}{f_1^2 - f_2^2}\lambda_1\,\phi_1 + \frac{2f_2^2}{f_1^2 - f_2^2}\lambda_2\,\phi_2 = M_1 + C + \varepsilon_1$$

C is a scaled linear combination of the carrier phase biases. As long as there are no cycle slips, *C* is a constant bias and of no intrinsic interest. In future discussion, it will be assumed that a mean value has been removed from computed values of MP_1. Note also that ε_ϕ and the carrier phase multipath terms have been dropped. This is because are 1-2 orders of magnitude smaller than the equivalent pseudorange terms.

4.2 Example of MP_1 for one satellite track

312 Equations (6)-(8) are defined at the time a GPS signal is received on the Earth. For any given
313 GPS receiver that records measurements every 15 seconds, there are thousands of MP_1
314 measurements per day per satellite. We use the satellite track highlighted in Figure 1 to
315 demonstrate some of the features of MP_1 data (Figure 5). The satellite rises in the northwest and
316 sets in the southwest several hours later; we split it into a northwest track and a southwest track
317 (Figures 5A and B). For elevation angles greater than 20 degrees, the MP_1 time series for this
318 satellite track is dominated by a white noise process, with a somewhat larger RMS in the
319 northwest than in the southwest portion. There is no obvious evidence of the multipath effects
320 that were shown in section 4. However, at low elevation angles (Figure 5C), the northwest track
321 is dominated by high-frequency, high-amplitude oscillations. These observations are consistent
322 with multipath predictions for a reflector height of ~40m (Figure 4, bottom panel). In contrast, at
323 best there is only a weak multipath signal as the satellite sets in the southwest (Figure 5D). Since
324 the same satellite transmitted the signal (satellite 1) and the same receiver (P048) recorded the
325 data, the source of the difference must be related to the terrain at the site. Recall, that it is
326 geometry (i.e. reflector heights) that controls pseudorange multipath frequencies, not vegetation.
327 The latter only impacts pseuodorange multipath amplitudes.

328 The digital elevation map (Figure 2C) for P048 provides insight as to the source of the
329 differences. P048 site is located on a hill. To the northwest, there is a flattening in the terrain
330 ~100m from the antenna. This region is locally planar and ~40m below the antenna. In contrast,
331 reflections from satellites rising/setting in the northeast, at the same elevation angles (10-15
332 degrees) and at the elevation difference, are not observed. This is because the hill blocks the
333 antenna from receiving the far reflections from the northeast.

334 In contrast, the terrain to the southwest has a fairly gentle slope. Forward models using the DEM
335 for this site indicates that the terrain southwest of the antenna is consistent with a nominal
336 reflector height of ~2 m [51]. We can also see in Figure 5C that the amplitude of the MP_1
337 oscillations is significantly smaller in the late spring than was observed in early spring. Since we
338 know that GPS has a repeating ground track (section 2), this decrease in MP_1 amplitude between
339 early and late spring must be caused by a decrease in the multipath reflection coefficient α. This
340 change is consistent with an increase in vegetation water content between the two dates. The
341 southwest satellite track shows no obvious variation in α between early and late spring because
342 the multipath error is small compared to the measurement error ε_1.

343 **4.3 Defining A Multipath Reflection Metric**

344 We seek a precise GPS reflection metric based on MP_1 that is (1) sensitive to the reflectivity (and
345 thus vegetation cover) of the ground and (2) representative of the vegetation surrounding each
346 site. Since MP_1 time series vary to first order as αD (recall that D is the excess path length), the
347 RMS of an individual MP_1 time series will also depend on αD (accomplishing goal 1). Recalling
348 the expansive azimuthal coverage of the GPS constellation (Figure 1A), an average of the all the
349 satellite MP_1 RMS data fulfills goal 2. A database of daily mean MP_1 RMS statistics for each site
350 is routinely compiled by the operators of PBO [53]; hereafter we will call this statistic MP_1rms,
351 as in [39]. The MP_1rms is a weighted mean, i.e. it is weighted by the number of observations for
352 each satellite.

353

354 For a L-band bi-static radar, we expect that MP_1rms in western Montana (the location of P048)
355 will be largest in early spring (when vegetation has low water content) and smaller in early

summer (when vegetation water content peaks). This hypothesis is supported by the MP_1rms observations (Figure 6A). The individual satellite MP_1rms data also show the effects of terrain. Satellites 30, 10, 4, 5, and 29 all have very large MP_1rms values. These satellites also have the largest percentage of satellite observations from the northwest azimuths (i.e. Figure 5A).

Even though it is difficult to see any kind of multipath effect in the individual MP_1rms time series at flatter sites, we have still found it possible to detect seasonal signals by averaging over the entire constellation. PBO site P041, located south of Boulder, Colorado, is a "flat" site. The antenna is 2 m above the ground, and there is less than 20 cm of terrain relief over the nominal GPS footprint. In Figure 6B we plot individual satellite MP_1rms values for two days, one in early and the other late spring. The seasonal variations are not nearly as striking as they were for P048. For a few satellites, the ground is more reflective in late spring than early spring (e.g. satellite 24). But overall, there are many more that follow the expected behavior of vegetation water content, high MP_1rms in early spring and low MP_1rms in late spring. We have found that by using averages of the individual satellite MP_1rms time series, vegetation signals are detectable at more than 300 PBO sites. Before these MP_1rms data can be used for phenological studies, we must first address the issue of outliers caused by snow and rain.

4.4 Outlier detection

A typical time series of daily MP_1rms values is shown in Figure 7A. The six-year MP_1rms time series shows similar behavior as 16-day NDVI data (Figure 7D). However, there is significant scatter in the winter and late fall that appears to be more episodic in nature. Many – but not all – of these outliers are coincident with near-zero NDVI values, i.e. they are consistent with snow cover.

Because GPS is a L-band system, GPS reflections will be sensitive to water within and on the surface of vegetation, as well as water in soil and snow. It is this very sensitivity that is being used by other terrestrial hydrology investigators [26,27,36,37,38,53,54,55]. To isolate the vegetation signal, MP_1rms data impacted by snow and very wet soil must be removed. We used the [56] dataset of climatological monthly snow water equivalent to identify times when snow was likely; data from those months were removed (Figure 7B). This is an overly conservative data editor; an improved snow filter is being developed that uses measured snow-extent observations from MODIS. The remaining outliers in the MP_1rms data are mostly related to early or late snowstorms or rainfall. Modeled temperature and precipitation data from the North American Land Data Assimilation System (NLDAS) were used to identify these early/late snowfall events and rainfall [57]. Snow events were defined based on the minimum NLDAS temperature and the daily precipitation value being greater than 2 mm. For small rain events (5-10 mm), that day was removed. For larger rain events (> 10mm), both the day it rained and the following day were removed. Finally, a two-week running mean was used to identify and remove three-standard deviation outliers. The resulting MP_1rms data are shown in Figure 7C.

4.5 Normalization

The MP_1rms results for site P048 shown in Figure 7C are consistent with those presented by [39], although the time series is now six years long instead of three years. Outliers present in that initial study are now much less frequent. Changes in NDVI strongly correlate (~-0.8) with changes in MP_1rms at P048 (Figure 7D). This is the case at many other PBO sites, although MP_1rms changes in the P048 eco-region typically lag those observed in NDVI by 1-3 weeks. Since the MP1rms values are influenced by the excess path length term D in equation (4),

MP_1rms time series from different GPS sites cannot be directly compared with each other. For example, at a flat site (P041), the largest MP_1rms values are ~0.28 m; at the hilly site, P048, the largest values are ~0.37 m. This does not mean that P048 has vegetation water content that is 32% (the ratio of 0.37/0.28) larger than for P041. In order to remove the first-order terrain effect caused by the excess path delay, we use a normalization (Normalized Microwave Reflection Index, NMRI) that scales MP_1rms by its maximum value. The latter represents the best estimate of when the signal is being reflected by the land surface with the minimum amount of vegetation water content. In Figure 7C, the maximum MP_1rms (shown by the dashed line) is based on the average of the largest 5% daily MP_1rms values. A negative ratio is used so that NMRI follows the vegetation growth cycle, i.e. NMRI increases as vegetation water content increases and vice versa.

(9)

$$NMRI = \frac{-(MP_1 rms - \max(MP_1 \text{rms}))}{\max(MP_1 \text{rms})}$$

In paper II, we show that this normalization yields a consistent relationship between NMRI and *in situ* measured vegetation water content across four GPS sites in Montana.

4.6 Footprint

Ordinarily the footprint of a remote sensing technique would be described before showing results using the technique. Here we have first developed simple theoretical descriptions of the method and showed representative results so that the footprint would be seen in that context. If all GPS sites were located in flat terrain, it would be straightforward to define the NMRI footprint (see,

419 e.g., the appendix of [58]). The Fresnel zone for a single rising or setting satellite track (for a
420 typical antenna height) is an ellipse, ~22 m in length (starting close to the antenna), but quite
421 narrow (~4m from side to side). By using the entire constellation, the flat-terrain footprint
422 basically mimics the first satellite coverage plot we showed (see Figure 8). The pie-shaped
423 region removed from the footprint represents the lack of satellites transmitting from the azimuth
424 angles -30 to 30 degrees. The radius of this site footprint (~22m) depends directly on the antenna
425 height H, ~2*H/tan(e), where e is the minimum elevation angle of 10 degrees and H is here
426 assumed to be 2m. The area of the flat-terrain footprint is ~1000 m^2. If the GPS antenna were
427 deployed on a 10 m tower over flat terrain, the site footprint would have a radius of ~115 m and
428 a correspondingly larger footprint area. However, there are no such tower-mounted sites in the
429 PBO network (Figure 2).
430
431 What about a site like P048, where we know there are reflections coming a vertical distance
432 greater than 2m? We have used a modified version of [51] to calculate the footprint of reflections
433 for P048 using the digital elevation map (Figure 2C). In addition to the central footprint already
434 discussed, this simulation shows a large circular footprint ~150 meters away from the antenna.
435 The area of this "hotspot" is in fact larger than the central footprint. The NMRI measurement
436 thus includes the effects of both reflection areas, but is dominated by the far reflections. This
437 means that each NMRI site will have its own footprint. For example, at some GPS sites there
438 will be hotspots to the east of the GPS antenna and at other GPS sites they will be to the south.
439 Some GPS sites will have more than one hotspot. The location and size of the hotspot(s) depends
440 on the vertical height of the planar surface with respect to the antenna. It will also depend on
441 whether these local planar surfaces produce reflections that can be observed at the antenna.

These hotspots are most easily mapped out with an electromagnetic simulation software. Such an analysis requires a DEM. Because of the way a GPS receiver's tracking loop has been programmed, no reflected signals can be observed that are delayed more than 300 m. Therefore, the maximum distance of reflections contributing to NMRI is 300 m from the antenna. Thus unlike a satellite remote sensing system, NMRI does not have one pixel size. It has a variable footprint that will yield useful phenological metrics if the footprint is representative of the ecosystem surrounding the antenna. An initial study of 305 NMRI time series found significant correlations with vegetation optical depth estimates at 90% of the sites, suggesting that the PBO network does have sensing zones that are representative of the regional ecosystems [58].

5. Discussion

Reflected signals measured by GPS ground receivers sense variations that are consistent with vegetation growth. These GPS reflection measurements are calculated on a daily basis and are unaffected by atmospheric effects such as clouds. The spatial footprint of the method depends on the terrain at the site, with a minimum footprint of 1,000 m^2. Methods have been developed to remove errors caused by snow and rain. A preliminary NMRI database has been compiled and consists of ~330 time series spanning the years 2007-2013 (http://xenon.colorado.edu/portal). A landcover classification is provided for each site. The bulk of the sites are grasslands, shrublands, and savannas (146, 74, and 70 sites, respectively). Since the purpose of the GPS network was to precisely measure the position of the ground, very few of the NMRI sites are located in heavily forested regions, as trees degrade positioning accuracy. It is expected that PBO will be maintained by NSF until at least 2020, providing an opportunity to measure the vegetation response to climate variability in the western United States over ~15 years. We plan to add

NMRI data for ~50 more sites to the data portal, with most of the new sites coming from desert ecosystems and Alaska. Surface soil moisture content and snow depth are provided for ~150 GPS sites using similar GPS reflection methods [54,55].

Here we have not linked the observed fluctuations in NMRI to changes in any particular biophysical parameters. In paper II, we show that NMRI correlates with vegetation water content measured *in situ* at four sites and correlates strongly with NDVI at 12 sites. All these comparison sites are located in Montana grasslands.

We make five final observations about NMRI:

1. NMRI is based on average MP_1rms records for each GPS satellite. Other normalizations, such as azimuthally binned MP_1rms data, should also be examined.
2. The algorithm to remove snow-contaminated values is conservative, which results in significant data removal during the winter. The definition of maximum MP_1rms can be improved by using satellite products to determine snow cover instead of climatology models.
3. NMRI is sensitive to variations of α from the multipath equation (4). It is not expected that α will directly relate to vegetation water content exactly the same way for different vegetation types. Models for electromagnetic scattering for different vegetation structures should be examined to aid in future normalizations [59].
4. All pseudorange data recorded by geodetic GPS receivers are impacted by multipath reflections. That being said, studies should be undertaken to compare pseudorange multipath recorded by different receiver manufacturers in order evaluate the possibility of receiver-dependent biases.

5. GPS reflections are impacted by both soil moisture and vegetation growth. We are able to reliably remove the effects of soil moisture in this study because it has a smaller effect on the pseudorange observables than vegetation growth.

6. Conclusions

The EarthScope Plate Boundary Observatory was designed and deployed to measure deformation caused by tectonic forces. Here we have shown that these same GPS instruments are sensitive to changes in vegetation state. There are over 10,000 GPS receivers around the world providing data to public archives. Although some of these GPS sites are located in urban areas, many could provide invaluable data for phenological research at very low cost. However, the locations of these sites will always be determined by the primary operator of the network. In the example used in this paper, the site selection was directed by geophysicists. The GPS technology used in this study is commercially available and can be installed by investigators at individual ecosystem study areas, but it would be more useful for phenology if the GPS antennas were deployed on towers. This would provide a large, homogeneous footprint for phenology studies and would complement satellite methods. Since many scientists use differential GPS to locate field sites, such a tower-mounted GPS site could also serve as a base station.

7. Acknowledgements

This research was funded by EAR-0948957, AGS-0935725, EAR-1144221, and NNX12AK21G. At UNAVCO we thank Lou Estey, Fran Boler, and Karl Feaux. John Braun, Felipe Nievinski, Ethan Gutmann, John Pratt, Andria Bilich, and Praveen Vikram provided assistance for this project. Some of this material is based on data, equipment, and engineering services provided by

the Plate Boundary Observatory operated by UNAVCO for EarthScope and supported by the National Science Foundation (EAR-0350028 and EAR-0732947). All GPS data used in this study are archived at UNAVCO. NMRI time series can be downloaded from http://xenon.colorado.edu/portal.

8. References

1. P. Kramer and J. Boyer, *Water Relations of Plants and Soils*, Academic Press, 495 pp, 1995.

2. S.L. Ustin, D.A Roberts, and J. Pinzón, "Estimating Canopy Water Content of Chaparral Shrubs Using Optical Methods," *Remote Sens. Environ*, vol. 65, pp. 280-291, 10.1016/S0034-4257(98)00038-8, 1998.

3. E.G. Njoku and S.K. Chan, "Vegetation and surface roughness effects on AMSR-E land observations," *Remote Sens. of Environ*., vol. 100, pp. 190-199, 10.1016/j.rse.2005.10.017, 2006.

4. D. Entekhabi, et al., "The Soil Moisture Active Passive (SMAP) Mission." *Proc. IEEE* vol. 98, pp. 704-716, 2010.

5. C.J. Tucker, "Red and photographic infrared linear combinations for monitoring vegetation," *Rem. Sens. Environ*., vol. 8, pp. 127-150, doi:10.1016/0034-4257(79)90013-0, 1979.

6. A.R. Huete, "A soil-adjusted vegetation index (SAVI)," *Remote Sens. Environ*., vol. 25, pp. 295–309, doi:10.1016/0034-4257, 1988.

7. G. Gutman and A. Ignatov, "The derivation of the green vegetation fraction from NOAA/AVHRR data for use in numerical weather prediction models," *Intern. Journ. Remote Sens.*, vol 19, pp. 1533−1543, 1998.

528 8. J. M. Paruelo, H. E. Epstein, W. K. Lauenroth, and I. C. Burke, "ANPP estimates from NDVI
529 for the central grassland region of the United States," *Ecology*, vol. 78, pp. 953–958,
530 10.1890/0012-9658, 1997.
531 9. B.K. Wylie, D.J. Meyer, L.L Tieszen, and S. Mannel, "Satellite mapping of surface
532 biophysical parameters at the biome scale over the North American grasslands: A case
533 study," *Remote Sens. Environ*., vol. 79, pp. 266-278, 10.1016/S0034-4257(01)00278-4, 2002.
534 10. D. Chen, J. Huang, and J.T. Jackson, "Vegetation water content estimation for corn and
535 soybeans using spectral indices derived from MODIS near- and short-wave infrared bands,"
536 *Remote Sens. Environ*., vol. 98, 225-236, doi: 10.1016/j.rse.2005.07.008, 2005.
537 11. P. Ceccato, S. Flasse, and J. Grégoire, "Designing a spectral index to estimate vegetation
538 water content from remote sensing data: Part 2. Validation and applications," *Remote Sens.*
539 *Environ*, vol. 82, pp. 198-207, 10.1016/S0034-4257(02)00036-6, 2002.
540 12. B. Gao, "NDWI-A normalized difference water index for remote sensing of vegetation liquid
541 water from space," *Remote Sens. Environ*., vol. 58, pp. 257-266, doi:10.1016/S0034-
542 4257(96)00067-3, 1996.
543 13. L. Serrano, S.L. Ustin, D.A. Roberts, J.A. Gamon, and J. Peñuelas, "Deriving Water
544 Content of Chaparral Vegetation from AVIRIS Data," *Remote Sens. of Environ*., vol. 74, pp.
545 570:581, 10.1016/S0034-4257(00)00147-4, 2000.
546 14. P. Ceccato, N. Gobron, S. Flasse, B. Pinty, and S. Tarantola, "Designing a spectral index to
547 estimate vegetation water content from remote sensing data: Part 1: Theoretical approach,"
548 *Remote Sens. Environ*., vol. 82, pp. 188-197, 10.1016/S0034-4257(02)00037-8, 2002.

549 15. T.J. Jackson, D. Chen, M. Cosh, F. Li, M. Anderson, C. Walthall, P. Doriaswamy, and E.R.
550 Hunt, "Vegetation water content mapping using Landsat data derived normalized difference
551 water index for corn and soybeans," *Rem. Sens. Environ*., vol. 92, pp. 475-482, 2004.
552 16. F.T. Ulaby, T.R. Moore, and A.K. Fung, *Microwave remote sensing: Active and passive, Vol.*
553 *III., from theory to applications*, Norwood Artech House, 1981.
554 17. T.J. Jackson and T.J. Schmugge, "Vegetation effects on the microwave emission of soils,"
555 *Remote Sens. of Environ.,* vol. 36, pp. 203-212, 1991.
556 18. M.O. Jones, J.S. Kimball, E.E. Small, and K.M. Larson, "Comparing Land Surface
557 Phenology Derived from Satellite and GPS Network Microwave Remote Sensing," *Int. Journ.*
558 *Biometeor.*, doi:10.1007/s00484-013-0726-z, 2013.
559
560 19. T.W. Brakke, E.T. Kanemasu, J.L. Steiner, F.T. Ulaby, and E. Wilson, "Microwave radar
561 response to canopy moisture, leaf-area index, and dry weight of wheat, corn, and sorghum,"
562 *Rem. Sens. Environ*., vol. 11, pp. 207–220, 10.1016/0034-4257(81)90020-1, 1981.
563 20. M.J. Hill, G.E. Donald, and P.J. Vickery, "Relating Radar Backscatter to Biophysical
564 Properties of Temperate Perennial Grassland," *Rem. Sens. Environ*., vol. 67, pp. 15–31, 1999.
565 21. S. Paloscia, G. Macelloni, P. Pampaloni, and E. Santi, "The contribution of multitemporal
566 SAR data in assessing hydrological parameters," *IEEE Geosci. Remote Sens. Lett*., vol. 1, pp.
567 201–205, 10.1109/LGRS.2004.831687, 2004.
568 22. R.D. De Roo, F.T. Ulaby, and M.C. Dobson, "A semi-empirical backscattering model at L-
569 band and C-band for a soybean canopy with soil moisture inversion," *IEEE Trans. Geosci*
570 *Remote Sens.*, vol. 39, pp. 864-872, 2001.

571 23. Y. Kim, J.T. Jackson, R. Bindlish, H. Lee, and S. Hong, "Radar vegetation indices for
572 estimating the vegetation water content of rice and soybean," *IEEE Geosci. Remote Sens.*
573 *Lett.*, vol. 9, pp. 564-568, doi:10.1109/LGRS.2011.2174772, 2012.
574 24. Y. Kim and J.J. van Zyl, "A Time-Series Approach to Estimate Soil Moisture Using
575 Polarimetric Radar Data," *IEEE Trans. Geosci. Remote Sens*. Vol. 47, pp. 2519-2527, 2009.
576 25. M. Martin-Neira, "A passive reflectometry and interferometry system (PARIS): application
577 to ocean altimetry," *ESA Journal***,** vol. *17*, pp. 331-355, 1993.
578 26. D. Masters, P. Axelrad, S. Katzberg, "Initial results of land-reflected GPS bistatic radar
579 measurements in SMEX02," *Remote Sens. of Environ.*, vol. 92, no. 4, pp. 507-520,
580 doi:10.1016/j.rse.2004.05.016, 2002.
581 27. S. Katzberg, O. Torres, M. Grant and D. Masters, "Utilizing calibrated GPS reflected signals
582 to estimate soil reflectivity and dielectric constant: Results from SMEX02," *Rem. Sens.*
583 *Environ*., vol. *100*(1), pp. 17-28, 2006.
584 28. S.T. Lowe, C. Zuffada, Y. Chao, P. Kroger, L.E. Young, J.L. LaBrecque, "5-cm-precision
585 aircraft Ocean altimetry using GPS reflections, *Geophys Res Lett*, vol. 29, no. 10,
586 doi:10.1029/2002GL014759, 2002.
587 29. H. Carreno-Luengo, H. Park, A. Camps, F. Fabra, A. Rius, "GNSS-R Derived Centimetric
588 Sea Topography: An Airborne Experiment Demonstration," *IEEE JSTARS*, vol. 6, no. 3,
589 1468-1478, 2013.
590 30. J.L. Garrison, A. Komjathy, V.U. Zavorotny, S.J. Katzberg, "Wind speed measurement using
591 forward scattered GPS signals," *IEEE Trans Geosci Remote Sens*, vol. 40, no. 1, pp. 50–65,
592 2002.

31. A. Komjathy, J.A. Maslanik, V.U. Zavorotny, P. Axelrad, S.J. Katzberg, “Sea ice remote sensing using surface reflected GPS signals,” In: Proceedings of the IEEE international geosciences and remote sensing symposium (IGARSS 2000), Honolulu, Hawaii, 2428 July, pp 2855-2857, 2000.

32. E. Valencia, A. Camps, N. Rodriguez-Alvarez, H. Park, I. Ramos-Perez, “Using GNSS-R Imaging of the Ocean Surface for Oil Slick Detection,” *IEEE JSTARS*, vol. 6, no. 1, pp. 217-223, 2013.

33. M. Semmling, G. Beyerle, R. Stosius, G. Dick, J. Wickert, F. Fabra, E. Cardellach, S. Ribó, A. Rius, A. Helm “Detection of arctic ocean tides using interferometric GNSS-R signals,” *Geophys Res Lett*. Vol. 38, no. 4, doi:10.1029/2010GL046005, 2011.

34. K.M. Larson, R. Ray, F. Nievinski, and J. Freymueller, “The Accidental Tide Gauge: A Case Study of GPS Reflections from Kachemak Bay, Alaska,” *IEEE GRSL,* vol. 10, no. 5, pp. 1200-1205, doi:10.1109/LGRS.2012.2236075, 2013.

35. E. Cardellach, F. Fabra, A. Rius, S. Pettinato, S. D'Addio, “Characterization of Dry-snow Sub-structure using GNSS Reflected Signals,” *Remote Sen. Environ.*, vol. 124, pp. 122-134, 10.1016/j.rse.2012.05.012, 2012.

36. N. Rodriguez-Alvarez, A. Camps, M. Vall-Ilossera, X.Bosch-Lluis, A. Monerris, I. Ramos-Perez, E. Valencia, J. Marchan-Hernandez, J. Martinez-Fernandez, G. Baroncini-Turricchia, C. Perez-Gutierrez, N. Sanchez, "Land Geophysical Parameters Retrieval Using the Interference Pattern GNSS-R Technique," *IEEE Trans. Geo. Rem. Sens.*, vol.49, no.1, pp.71-84, doi:10.1109/TGRS.2010.2049023, 2011.

37. N. Rodriguez-Alvarez, X. Bosch-Lluis, A. Camps, A.Aguasca, M. Vall-Illossera, E. Valencia, I. Ramos-Perez, H. Park, "Review of crop growth and soil moisture monitoring

616 from a ground-based instrument implementing the Interference Pattern GNSS-R technique",
617 *Radio Sci.*, vol. 46., no. 6, doi:10.1029/2011RS004680, 2011.
618 38. A. Egido, M. Caparrini, G. Ruffini, S. Paloscia, L. Guerriero, N. Pierdicca, and N. Floury,
619 "Global Navigation Satellite System Reflectometry as a Remote Sensing Tool for
620 Agriculture ," Remote Sens. Vol. 4, pp. 2356-2372, doi:10.3390/rs4082356, 2012.
621
622 39. E.E. Small, K.M. Larson, and J.J. Braun, "Sensing Vegetation Growth with GPS
623 Reflections," *Geophys. Res. Lett.*, vol. 37, L12401, doi:10.1029/2010GL042951, 2010.
624 40. E.E. Small, K.M. Larson, and W. Smith, "Normalized Microwave Reflection Index, part II:
625 Validation of Vegetation Water Content Estimates Using from Montana Grasslands,"
626 JSTARS *IEEE, submitted*.
627 41. D.C. Agnew and K.M. Larson, "Finding the Repeat Times of the GPS Constellation, *GPS*
628 *Solutions*," vol. 11, pp. 1-9, 2007.
629 42. W.H. Prescott, J.L. Davis, and J. L Svarc, "Global Positioning System measurements for
630 crustal deformation," *Science*, vol. 244, pp. 1337–1339, 1989.
631 43. J.M. Tranquilla, J.P. Carr, H.M. Al-Rizzo, "Analysis of a Choke Ring Groundplane for
632 multipath Control in GPS Applications," IEEE Trans. Antennas and Propagation, vol. 42, no.
633 7, pp. 905-811, 1994.
634 44. Y. Georgiadou and A. Kleusberg, "On carrier signal multipath effects in relative GPS
635 positioning," *Manusc. Geod.*, vol. 13, pp. 172-179, 1988.
636 45. P. Misra and P. Enge, *Global Positioning System: Signals, Measurements, and Performance*,
637 Revised 2nd edition, Ganga-Jamuna Press, Lincoln MA, 2011.
638 46. M.S. Braasch, "Multipath Effects," in Global Positioning System: Theory and Applications,

639 Vol. 1, Editors: B.W. Parkinson, J.J. Spilker Jr., P. Axelrad, P. Enge, AIAA, pp. 547-568,
640 1995.
641 47. J.K. Ray, M. E. Cannon, "Synergy between Global Positioning System code, carrier, and
642 signal-to-noise ratio multipath errors," *J.Guid. Control Dyn*., vol. 24, pp. 54–63, 2001.
643 48. P. Axelrad, K.M. Larson, and B. Jones, "Use of the Correct Satellite Repeat Period to
644 Characterize and Reduce Site-Specific Multipath Errors," *Proc. Inst. Of Navigation,* Long
645 Beach, CA, pp. 2638-2648, 2005.
646 49. A. Bilich, "Improving the Precision and accuracy of Geodetic GPS: Applications to
647 Multipath and Seismology," Ph.D. Dissertation, University of Colorado, 2006.
648 50. V. Zavorotny, K.M. Larson, J.J. Braun, E.E. Small, E. Gutmann and A. Bilich, "A physical
649 model for GPS multipath caused by ground reflections: toward bare soil moisture retrievals,"
650 *IEEE-JSTARS*, vol. 3, pp. 100-110, 10.1109/JSTARS.2009.2033608, 2010.
651 51. F.G. Nievinski and K.M. Larson, "A GPS multipath simulator for near-surface reflectometry
652 and positioning applications," *GPS Solutions*, 10.1007/s10291-013-0331-y, 2013.
653 52. C.C. Chew, E.E. Small, K.M. Larson, and V. Zavorotny, "Effects of Near-Surface Soil
654 Moisture on GPS SNR Data: Development of a Retrieval Algorithm for Volumetric Soil
655 Moisture," *IEEE Trans. Geosci Remote Sens*., doi:10.1109/TGRS.2013.2242332, 2013.
656 53. L. Estey and C. Meertens, "TEQC: The multi-purpose toolkit for GPS/GLONASS data,"
657 *GPS Solutions*, vol. 3, no. 1, pp. 42–49, 1999.
658 54. K.M. Larson, E.E. Small, E. Gutmann, A. Bilich, J. Braun, V. Zavorotny, "Use of GPS
659 receivers as a soil moisture network for water cycle studies," *Geophys. Res. Lett., vol. 35,*
660 L24405, doi:10.1029/2008GL036013, 2008.
661 55. K.M. Larson, E. Gutmann, V. Zavorotny, J. Braun, M. Williams, F. Nievinski, "Can We

662 Measure Snow Depth with GPS Receivers?" *Geophys. Res. Lett.*, vol. *36,* L17502,
663 doi:10.1029/2009GL039430, 2009.
664 56. R.L. Armstrong, M. J. Brodzik, K. Knowles, and M. Savoie, "Global Monthly EASE-Grid
665 Snow Water Equivalent Climatology," Version 1.0. Boulder, Colorado USA: National Snow
666 and Ice Data Center, 2007.
667 57. K.E. Mitchell, et al. "The multi-institution North American Land Data Assimilation System
668 (NLDAS): Utilizing multiple GCIP products and partners in a continental distributed
669 hydrological modeling system," *J. Geophys. Res.*, vol. 109, D07S90,
670 doi:10.1029/2003JD003823, 2004.
671 58. K.M. Larson and F.G. Nievinski, "GPS Snow Sensing: Results from the EarthScope Plate
672 Boundary Observatory," *GPS Solutions*, vol. 17, pp. 41-52, 2013.
673 59. C.C. Chew, E.E. Small, K.M. Larson, and V. Zavorotny, Utility and limitations of GPS
674 interferometric reflectometry for vegetation sensing, *IEEE TGRS,* acceptance pending
675 revision.
676

677 **Appendix I.**

678 Excellent summaries and discussions about the GPS pseudorange observable and multipath
679 effects can be found in [45,46,47]. Here we follow the descriptions provided by [48,49]. The
680 pseudorange multipath error (M) is directly related to the code tracking loop behavior and its
681 discriminator equation. In brief, a GPS receiver "tracks" by driving the difference between the
682 early and late discriminator spacing ($2T_{E/L}$) to zero. When no multipath is present (direct only,
683 Figure A1):
684

$$A1.\left[R\left(T_{E/L}\right) - R\left(-T_{E/L}\right)\right] = 0$$

where R represents the autocorrelation function of the code. However, multipath distorts the correlation function as the receiver must now track the composite signal (combined, Figure A1) while retaining correlator spacing $2T_{E/L}$. This results in shifted correlator values due to the multipath delay, and a new discriminator equation

$$A2.\left[R\left(M + T_{E/L}\right) - R\left(M - T_{E/L}\right)\right] + \alpha cos\varphi\left[R\left(M + T_{E/L} - D\right) - R\left(M - T_{E/L} - D\right)\right] = 0$$

where α is the ratio of the of the amplitudes of the reflected and direct signals and φ is the phase shift of the reflected relative to the direct signal and D is the path delay. If we assume that the autocorrelation function has an ideal triangular shape for multipath delays shorter than the chip length T

$$\text{A3.}\quad R(\tau) = 1 - \frac{|\tau|}{T}\ for\ |\tau| < T$$

we can reduce equation A2 to:

$$A4.\frac{-2M}{T} + \alpha cos\varphi\left(-2\frac{(M - D)}{T}\right) = 0$$

and subsequently:

$$A5.\ M = \frac{\alpha D cos\varphi}{1 + \alpha cos\varphi}$$

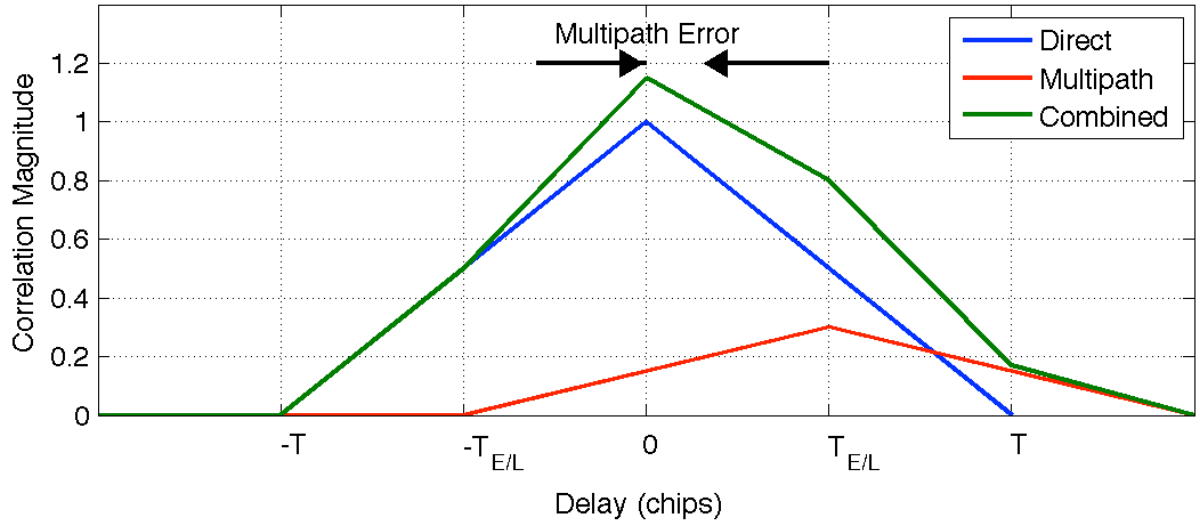

Figure A1. A cartoon depiction of how multipath impacts the observed pseudorange measurement. The x-axis is measured in chips. The direct signal has no multipath. A single multipath reflection (0.5 chip delay and a relative amplitude of 0.3) is shown in red. The receiver tracks the combined signal (green). The y-axis is the normalized correlation function.

716

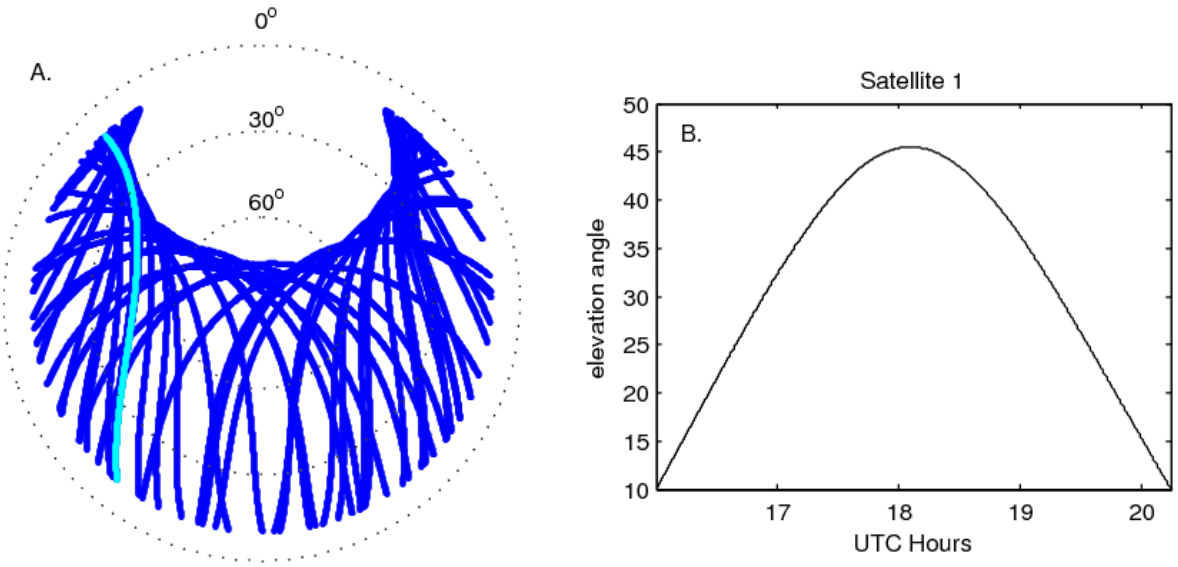

717

718 Figure 1. A. Polar plot representation of satellite azimuth and elevation angles for PBO site
719 P048, located in southern Montana. Concentric circles represent satellite elevation angles (the
720 angle with respect to the horizon). North is the top of the plot, east is to the right, etc. Note that
721 there are no GPS satellite tracks to the north. The track for satellite 1 is highlighted in cyan; B.
722 Time vs. elevation angle for satellite 1.

723

724

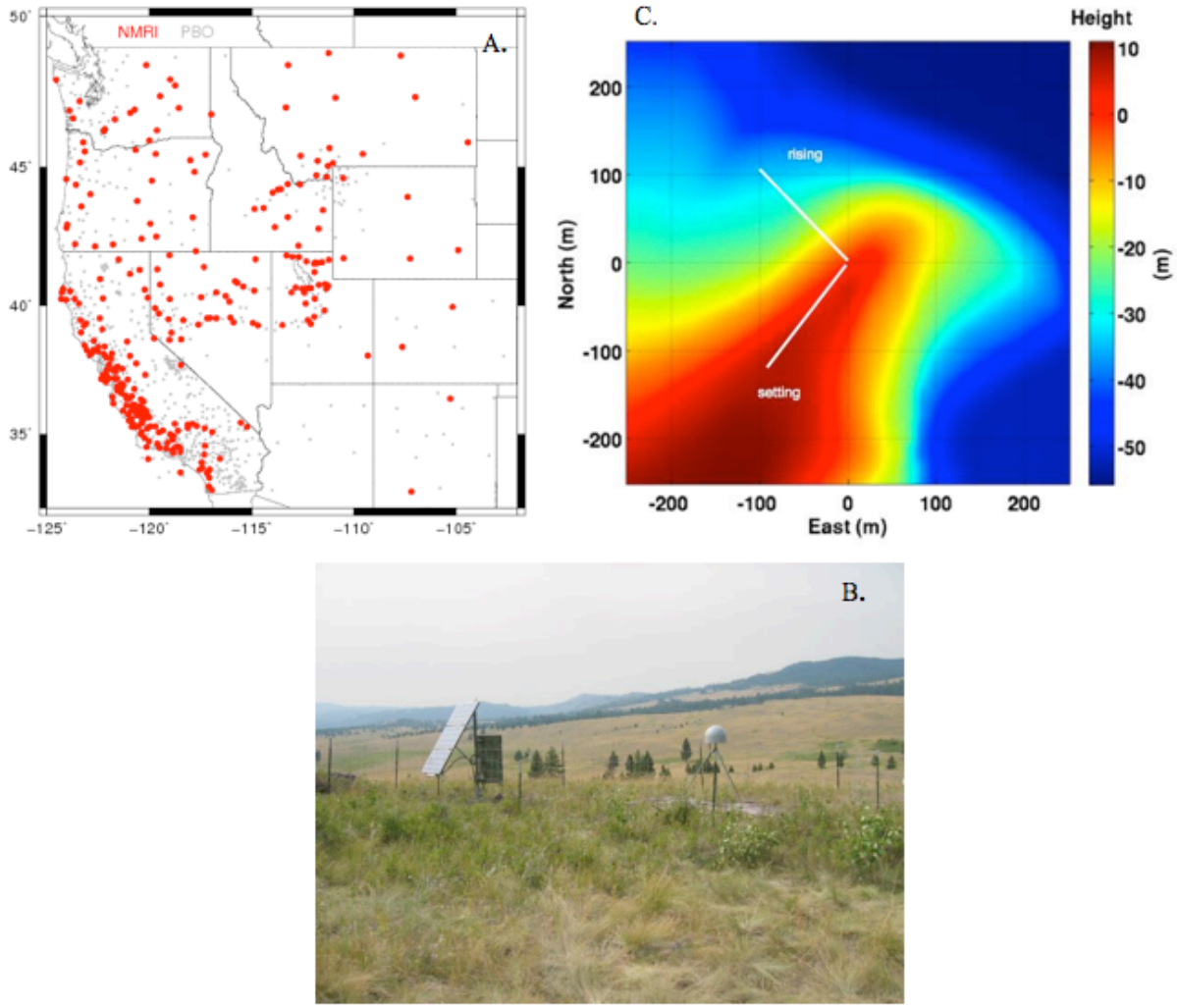

725

726 Figure 2A. Locations of GPS sites in the Plate Boundary Observatory (PBO) are shown in gray.
727 The sites with currently available NMRI time series are highlighted in red. An additional 150
728 PBO sites are in Alaska (30 NMRI sites); B. Typical setup at a continuously-operating PBO GPS
729 site in western Montana. The antenna (covered by an acrylic dome) is set atop a tripod
730 monument that has been drilled into the ground. A solar panel (and a bank of batteries) is used to
731 provide power for the system; C: Digital Elevation Map (DEM) for site P048. The ground track
732 for satellite 1 is shown in white.

733

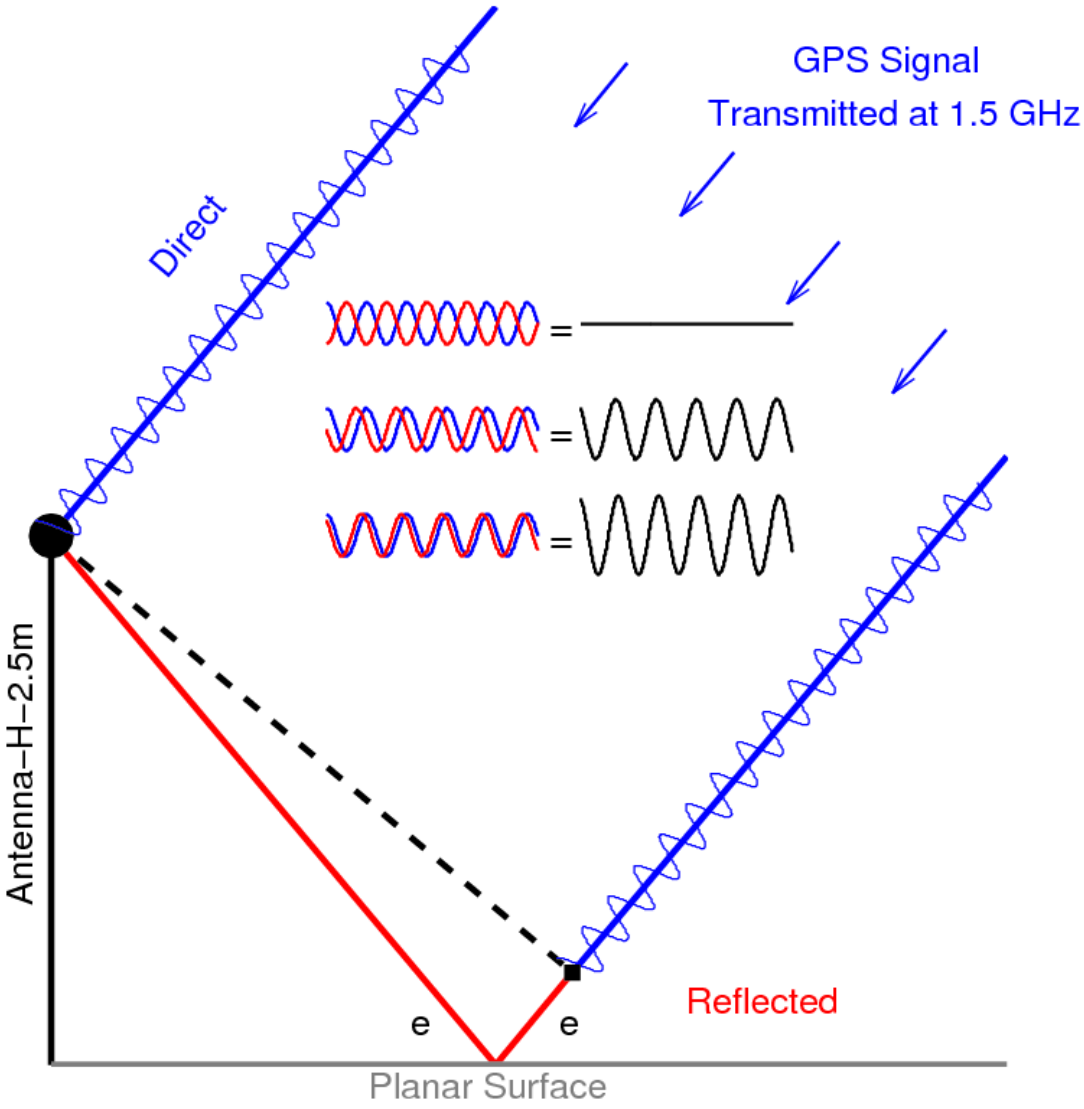

734

735

736 Figure 3. Each GPS satellite transmits a signal that arrives at an individual receiver on the Earth
737 as a plane wave. A planar reflector is shown in gray. The antenna is 2.5m above the reflecting
738 surface and represented by the black circle. The direct signal (blue) travels a shorter distance
739 than the reflected signal (blue plus red). The elevation angle of the satellite with respect to the
740 horizon is e. The GPS carrier signal (wavelength ~19 cm) is shown superposed on the direct
741 signal. Depending on the extra path travelled by the reflection (shown in red), the direct and

742 reflected signals will interfere (shown for three examples in the center of the figure). This
743 interference (shown in black) is what is measured by the GPS unit.
744
745

746

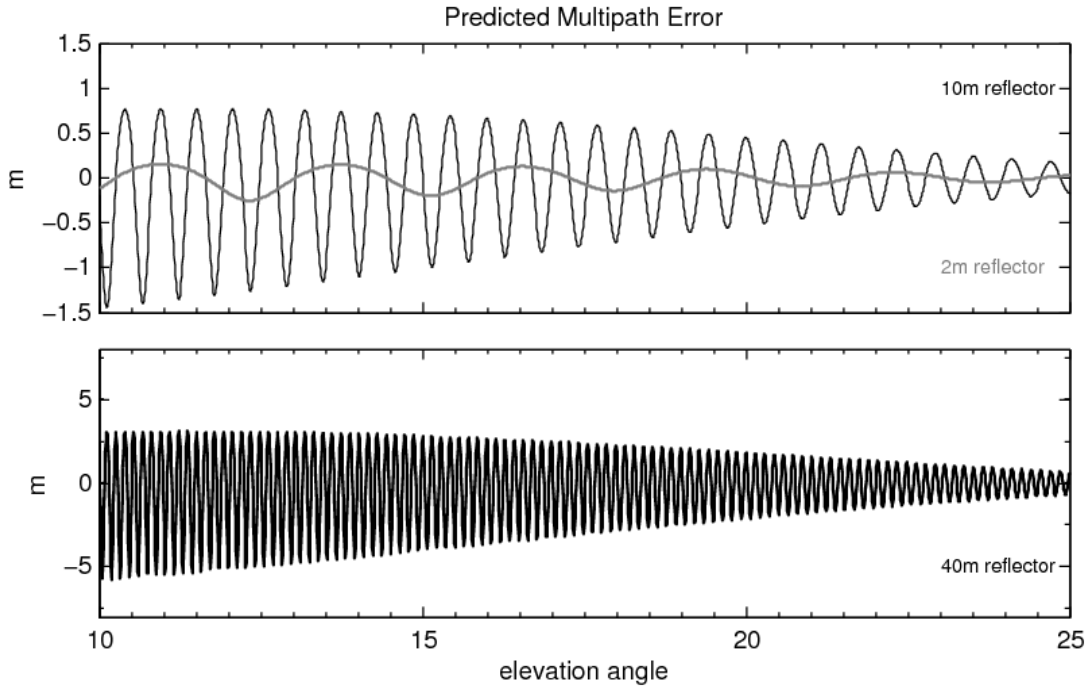

747

748

749 Figure 4. Predicted multipath errors for planar, horizontal reflectors at three vertical distances: 2,
750 10, and 40 m. Note the change in vertical scale. The α profile used for the predictions was
751 chosen to be consistent with GPS observations using PBO instrumentation, i.e. it exponentially
752 decays as elevation angle increases.

753

754

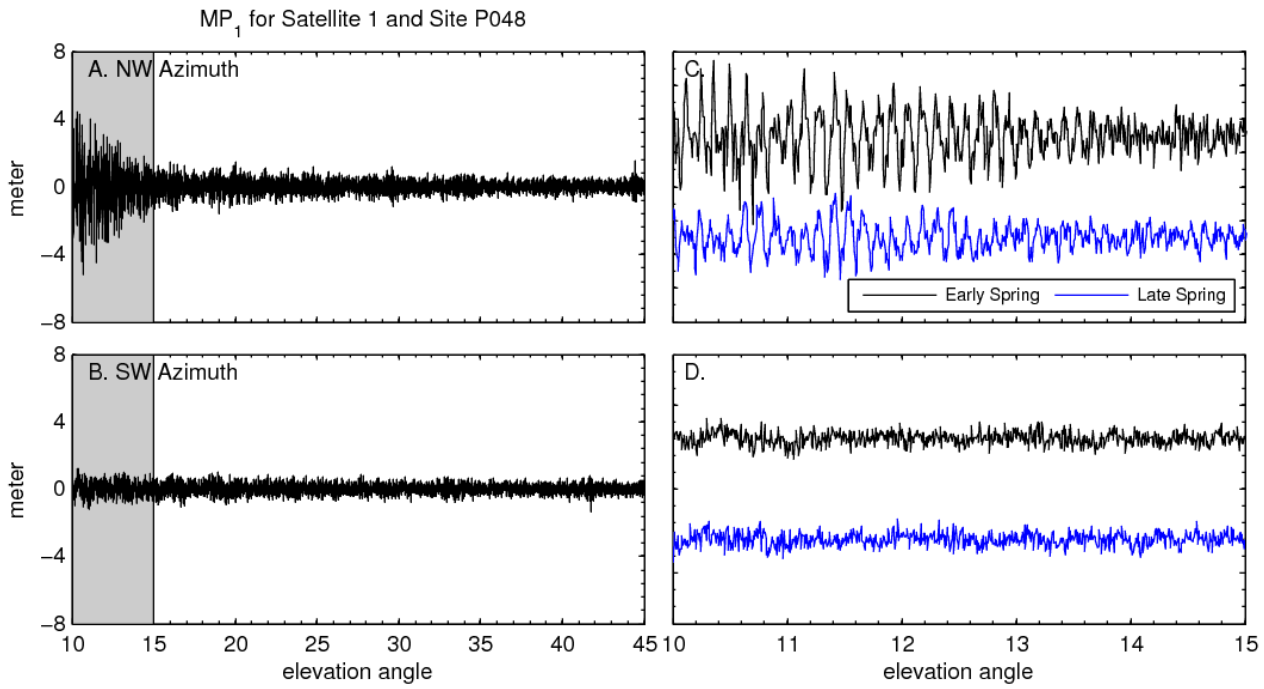

755

756 Figure 5. MP_1 data for site P048 and satellite 1; A. Rising arc (northwest azimuths); B. setting
757 arc (southwest azimuths); C. Lowest elevation angle data from panel A (shown in gray); D.
758 Lowest elevation angle data from panel B. Data in C and D are vertically offset to show data
759 from both late (blue) and early (black) spring.

760

761

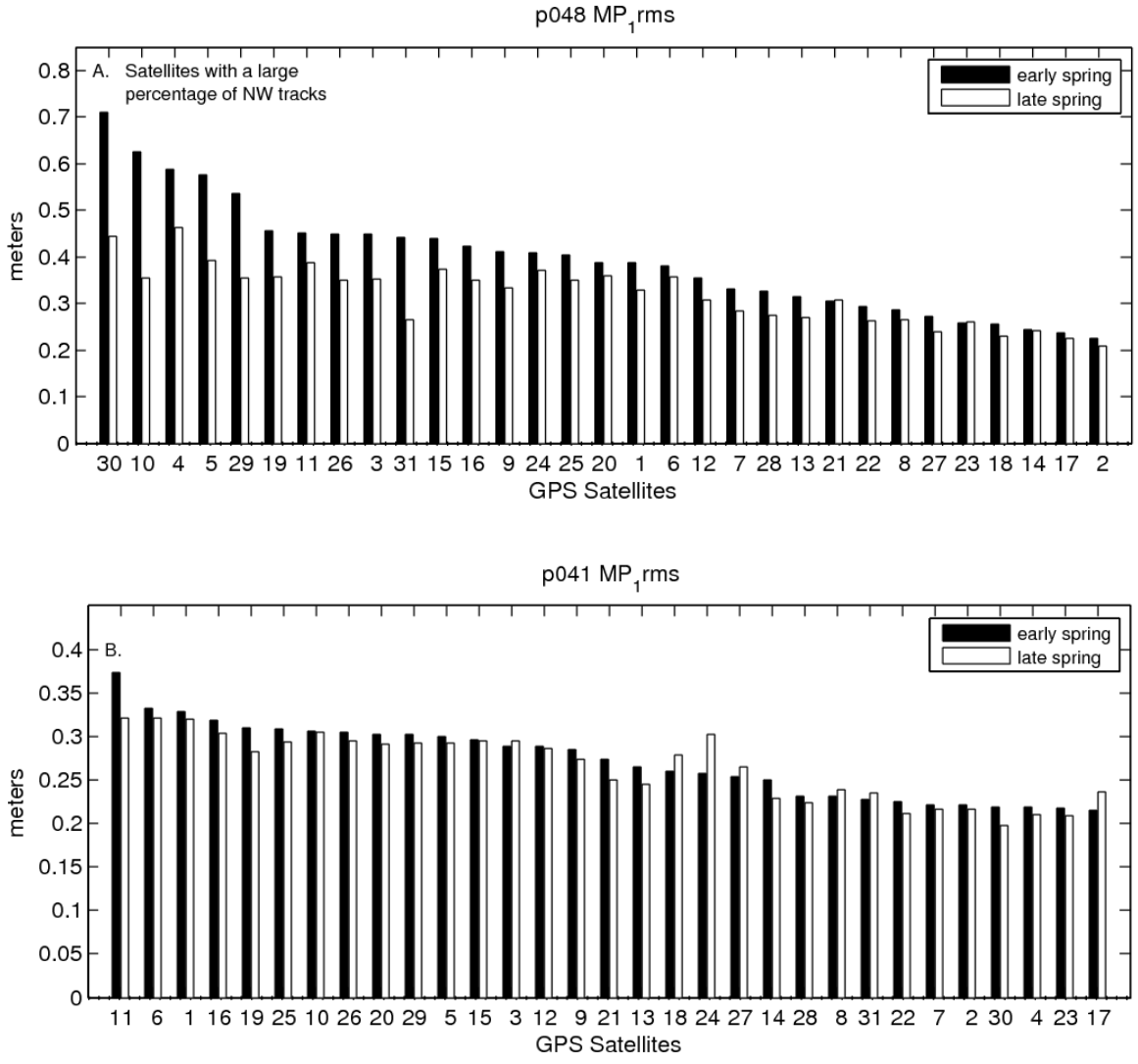

Figure 6. A. Station P048 MP1rms (ordered by magnitude) for individual GPS satellites for days in early and late spring; B. the same quantities for station P041, near Boulder, Colorado. GPS satellites are numbered from 1-31.

762

763

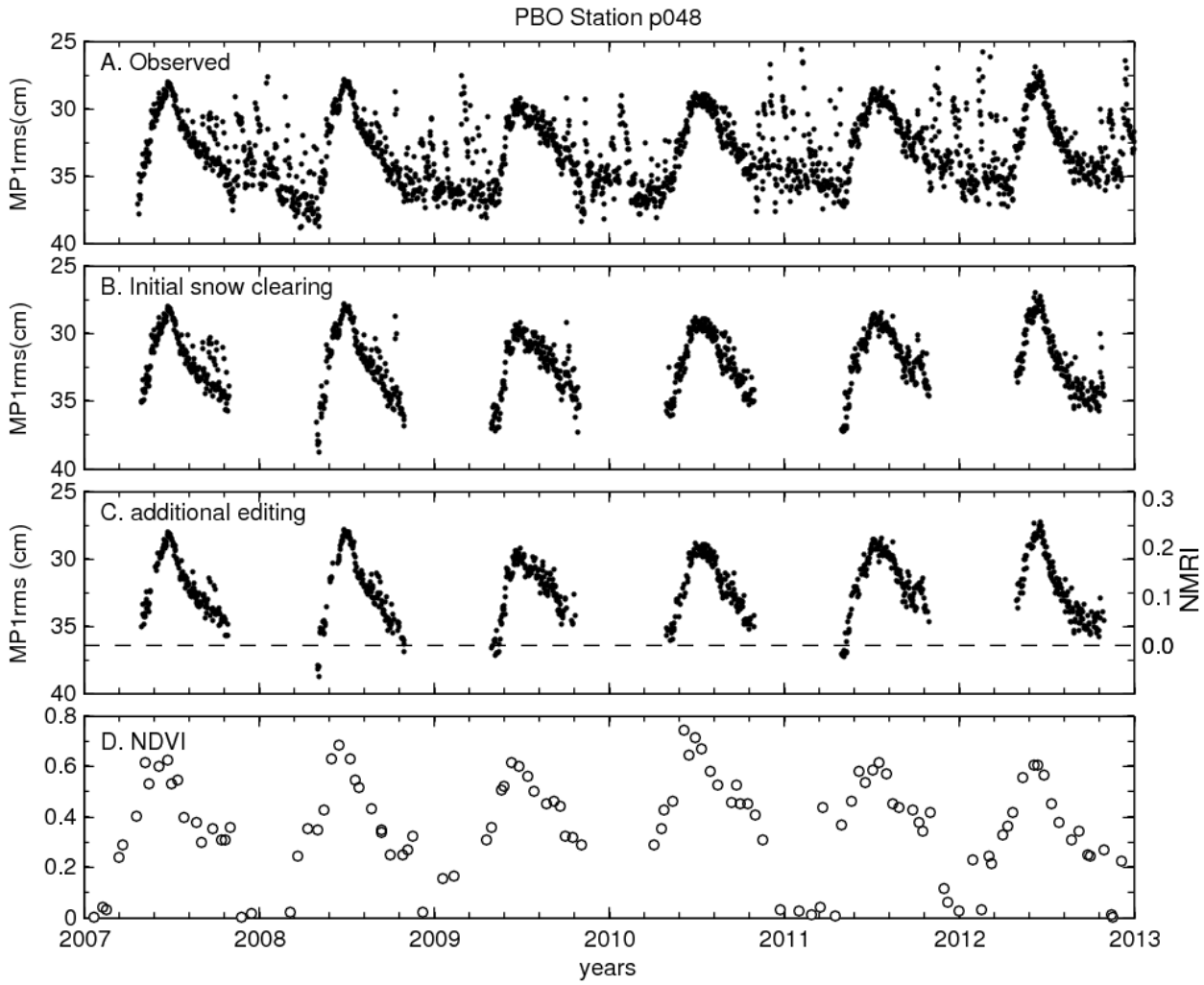

764

765 Figure 7. A. MP_1rms values for station P048 taken from the UNAVCO database (Estey and
766 Meertens, 1999); B. MP_1rms data after snow clearing using climatology model; C. final edited
767 MP_1rms time series, with NMRI values shown on the right y-axis; D. 16-day MODIS NDVI
768 product.

769

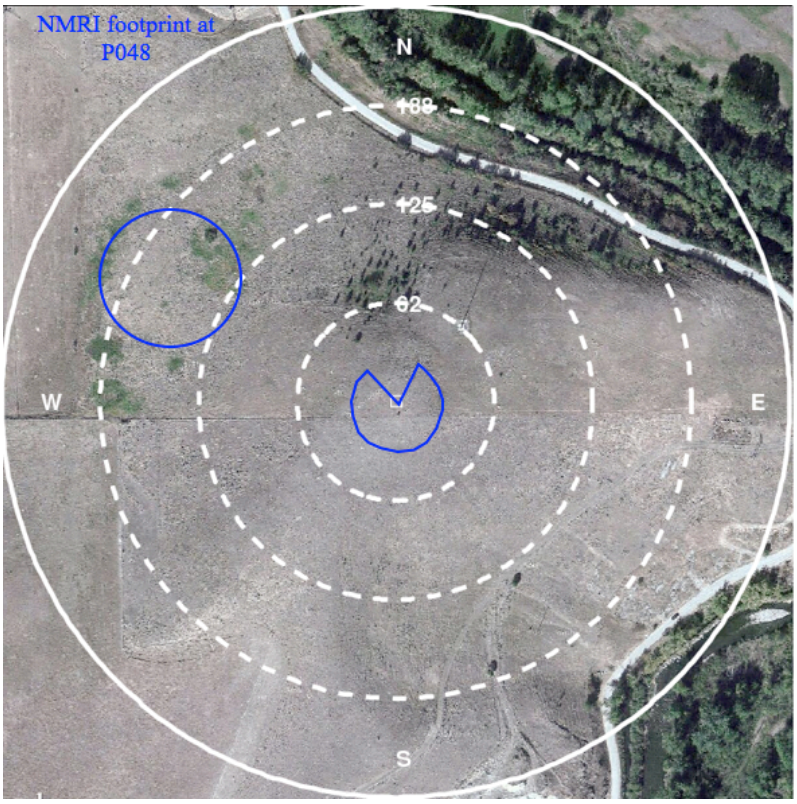

Figure 8. Footprint of the NMRI metric at GPS site P048. This site's footprint includes both near- reflections (central circle with pie shape removed) based on the ~2-meter antenna height and a large secondary footprint (hotspot) to the northwest caused by terrain differences. Image taken from Google Earth. Radial distances given in meters (62, 125, 168, 250) for the white circles.